Numerical Simulation of a Thermal-Hydraulic-Chemical Multiphase Flow Model for CO2 Sequestration in Saline Aquifers

Etienne Ahusborde, Brahim Amaziane, Fabrizio Croccolo, Nicolas Pillardou

Numerical simulation of a thermal-hydraulic-chemical multiphase flow model for CO_2 sequestration in saline aquifers

Etienne Ahusborde[1] Brahim Amaziane [1] Fabrizio Croccolo [2]
Nicolas Pillardou [1,2]

[1] Universite de Pau et des Pays de l'Adour, E2S UPPA, CNRS, LMAP, Pau, France.
[2]Universite de Pau et des Pays de l'Adour, E2S UPPA, CNRS, TotalEnergies, LFCR, Anglet, France.

Abstract

We consider a reactive multiphase multicomponent Darcy flow in a porous medium while taking into account the effects of temperature. This flow model is coupled to an energy balance equation and ordinary and/or algebraic differential equations to model the chemical reactions. The model is discretized using a cell-centered finite volume method with implicit Euler or second order backward differential formula time discretization. Both sequential and fully coupled fully implicit strategies are considered. Two new DuMu^X modules are developed based on the above schemes. Two numerical examples are presented to validate the implementation of the two methods and the capability of the code to solve CO_2 sequestration scenarios. The first test addresses a one-dimensional radial problem to study thermal effects on injectivity during CO_2 storage. For this purpose, isothermal/nonisothermal comparisons are carried out to highlight these differences, which can modify the flow. The second test is chosen to test the code to approximate solutions for a three-dimensional benchmark based on the Johansen CO_2 storage operation. Then, we compare the efficiency, performance in terms of computation time, and parallel scalability of the sequential and implicit methods. In conclusion, both modules demonstrate accuracy, numerical robustness and the potential to solve realistic problems. With an equal time step, the sequential scheme can be faster than the implicit scheme, but the splitting can present a loss of accuracy, particularly concerning the conservation of mass of the injected CO_2.

1 Introduction

Carbon capture and sequestration (CCS) in underground formations represents one of the most promising strategies to mitigate the effects of greenhouse gases (see, for instance, [30] and the references therein). Saline aquifers are considered formations with the highest storage potential, due to their global abundance [30]. Different geochemical and physical trapping mechanisms operating at different time and space scales must be combined to guarantee a high containment rate and long-term safety [26]. As a consequence, the numerical modeling and simulation of CCS has become crucial for assessing CO_2 migration in saline aquifers as well as potential leakage, at time scales of several thousand years [15]. Carbon storage is typically modeled by multiphase flow and multicomponent reactive transport to account for rock-fluid interactions in the subsurface [29, 30, 32]. Most studies have considered isothermal conditions by assuming that CO_2 is injected under ambient reservoir conditions, and, thus the coupling between flow and reactive transport is called hydraulic-chemical (HC) coupling (see, [9]

and the references therein). Numerous methods have been developed to perform numerical simulations of CO_2 storage for HC coupling. We refer to several books [15, 29, 30] and recent reviews of articles [9, 14, 21, 33]. Considering the effects of temperature can lead to an additional coupling called thermal-hydraulic-chemical coupling (THC), for which, few results have been obtained. However, according to [39] and [40], nonisothermal effects can play a major role in storage scenarios where the injectant stream temperature is significantly different from that of the reservoir and most critically for shallower storage reservoirs where CO_2 is close to its critical point. In [46], the authors concluded that considering nonisothermal processes is necessary to accurately assess the pressure rise in a near-well region during CO_2 injection. In [10], the authors showed that a low CO_2 injection temperature is an interesting approach to enhance well injectivity. We also noted that some authors coupled the THC processes with geomechanics and considered a coupled thermal-hydro-mechanical-chemical (THMC) model, see [17, 20, 23, 37, 44, 45] and the references therein. In these studies, most of the authors noted that thermal energy affects the mean stress and geochemical reactions and thus contributes to enhanced storage efficiency.

Traditionally, the solution schemes in numerical codes for reactive transport problems can be divided into three categories: the sequential iterative approach (SIA), sequential noniterative approach (SNIA) and global implicit approach (GIA). Recent reviews detailing the uses of industrial reservoir simulators and academic simulation platforms can be found in [7] and [36]. Sequential approaches decouple flow and reactive transport into two subproblems that are solved separately with an operator splitting method [38, 41, 44]. This splitting can generate mass conservation errors that can be reduced with the SIA. In contrast, the GIA solves a unique highly nonlinear problem, leading to fewer restrictions on the time step size and providing more accuracy, stability and robustness [35, 36, 45]. However, this approach becomes expensive in terms of computational cost for large chemical systems.

In recent years, we developed a sequential strategy in [8] and a fully coupled fully implicit approach in [9] using finite volume (FV) methods to solve isothermal reactive two-phase (HC) flows. Finite volume methods have been widely used in reservoir simulations due to their flexibility in dealing with complex geometries, their moderate computational cost and because, by construction, they are mass conservative. The two-point flux approximation (TPFA) [18] has been widely used in reservoir simulators for the petroleum industry. Nonetheless, this scheme presents some limitations on the type of mesh that can be used since it requires strict K-orthogonality. For more general meshes, multiple-point flux approximation (MPFA) [6] or the more recently developed nonlinear two-point flow approximation (NLTPFA) [34] can be used. In this study, given the nature of the meshes used, we adopted a cell-centered TPFA. In [34], the authors obtained very close results when using TFPA or NLTPFA on the same three-dimensional geometry that we consider in the following. Both sequential and fully implicit strategies have been validated on several test cases. This study aims to extend these two strategies to nonisothermal reactive two-phase flows (THC) using high-performance computing (HPC) tools and to compare them in the same numerical environment. For this purpose, we have developed sequential and fully coupled fully implicit algorithms within the framework of the parallel open-source platform DuMu^X[22]. Our numerical strategy combines the advantages of the TPFA method to accurately solve the diffusion terms with an upwind method for space discretization on regular or unstructured grids. The time discretization is achieved by an implicit Euler scheme or a second-order backward differential formula, since the latter has advantages over the former in cases, where the convective dissolution that arises from a fingering instability at the moving CO_2 groundwater interface. Finally, numerical examples of THC coupling for CO_2 storage in saline aquifers are presented, one of which is related to three-dimensional flow based on the Johansen reservoir.

The rest of the paper is organized as follows. Section 2 formulates the mathematical model used to describe THC coupling processes for CO_2 storage. In Sect. 3, a brief description of the sequential and fully implicit strategies used to solve nonisothermal two-phase flow coupled with reactive transport is given. The discretization of the system provided by the fully coupled fully implicit approach using

an FV scheme is also presented. In Sect. 4, a description of the implementation of our strategies in DuMu^X is given. Then, to validate our approach, we consider two test cases. The first addresses a one-dimensional radial problem to study thermal effects on injectivity during CO_2 storage. The second test case involves a highly heterogeneous three-dimensional formation. The latter aims at comparing sequential and implicit strategies using HPC and proving the ability of our approach to deal with realistic applications. Finally, conclusions and perspectives are offered in Sect. 5.

2 Mathematical model for THC processes

Generally, CO_2 storage problems are described as multiphase flow problems coupled with other processes depending on the envisioned complexity. In this work, we are mainly interested in THC processes, and this section is devoted to presenting the geochemical and mathematical models used to characterize nonisothermal two-phase multicomponent flows with reactive transport in porous media. In the following, we define $\alpha = \{l, g, s\}$ as the phase index, which stands for liquid, gaseous or solid phases, while the superscripts i and j denote components.

Before describing the geochemical model, it is necessary to define a framework that allows us to properly write the chemical interactions. First, let I represent the set of all N_c chemical species involved in the N_r chemical reactions. According to the Morel formalism [28], it is possible to split species between primary and secondary species. The primary species are chosen so that each secondary component can be written as a linear combination of the primary species. Consequently, I can be divided into I_p and I_s so that $I = I_p \cup I_s$. Then, each subset I_p and I_s is divided again into two sub-subsets that describe mobile and immobile species such as inert and reactive rocks. This splitting leads to $I_p = I_{pm} \cup I_{pi}$. For the secondary species, it is also possible to add species involved in the precipitation/dissolution equilibrium I_{se} and kinetic I_k reactions, so that $I_s = I_{sm} \cup I_{si} \cup I_{se} \cup I_{sk}$.

To address the sequential approach in which the two-phase flow is decoupled from reactive transport, two other subsets are introduced so that $I = I_{2\varphi} \cup I_{rt}$. The subset $I_{2\varphi}$ represents all species that are present in both liquid and gas phases, whereas I_{rt} consists of the remaining species.

A chemical reaction is therefore written in the form

$$\sum_{j=1}^{N_c} \nu_{ij} A_j \; = \; 0, \quad i = 1, \ldots, N_r, \tag{1}$$

where ν_{ij} and A_j refer to the stoichiometric coefficient and the chemical species, respectively.

To illustrate all the sets of species defined above, we provide an example of a chemical system in Table 1. Here, we consider eight reactions: two aqueous dissolutions, three aqueous complexation reactions at equilibrium, one mineral precipitation dissolution at equilibrium for calcite and two kinetic precipitation/dissolution reactions for anorthite and kaolinite.

Table 1: Example of chemical system

Reactions		
$H_2O_{(g)}$	$\rightleftharpoons$	$H_2O_{(l)}$
$CO_{2(g)}$	$\rightleftharpoons$	$CO_{2(l)}$
$OH^- + H^+$	$\rightleftharpoons$	$H_2O_{(l)}$
$CO_3^{2-} + 2\,H^+$	$\rightleftharpoons$	$H_2O_{(l)} + CO_{2(l)}$
$HCO_3^- + H^+$	$\rightleftharpoons$	$CO_{2(l)} + H_2O_{(l)}$
Calcite $+ 2\,H^+$	$\rightleftharpoons$	$Ca^{2+} + H_2O_{(l)} + CO_{2(l)}$
Anorthite $+ 8\,H^+$	$\rightleftharpoons$	$4\,H_2O_{(l)} + Ca^{2+} + 2\,Al^{3+} + 2\,SiO_2$
Kaolinite $+ 6\,H^+$	$\rightleftharpoons$	$5\,H_2O_{(l)} + 2\,Al^{3+} + 2\,SiO_2$

For this chemical system, the different chemical species can be divided as follows:

$$\begin{aligned}
I_{pm} &= \left\{\mathrm{H_2O_{(l)}}, \mathrm{CO_{2(l)}}, \mathrm{H^+}, \mathrm{Ca^{2+}}, \mathrm{Al^{3+}}, \mathrm{SiO_2}\right\}, \\
I_{pi} &= \{\varnothing\}, \\
I_{sm} &= \left\{\mathrm{H_2O_{(g)}}, \mathrm{CO_{2(g)}}, \mathrm{OH^-}, \mathrm{CO_3^{2-}}, \mathrm{HCO_3^-}\right\}, \\
I_{si} &= \{\varnothing\}, \\
I_{se} &= \{\text{Calcite}\}, \\
I_{sk} &= \{\text{Anorthite}, \text{Kaolinite}\}, \\
I_{2\varphi} &= \left\{\mathrm{H_2O_{(l)}}, \mathrm{H_2O_{(g)}}, \mathrm{CO_{2(l)}}, \mathrm{CO_{2(g)}}\right\}, \\
I_{rt} &= \left\{\mathrm{H^+}, \mathrm{Ca^{2+}}, \mathrm{Al^{3+}}, \mathrm{SiO_2}, \mathrm{OH^-}, \mathrm{CO_3^{2-}}, \mathrm{HCO_3^-}, \text{Calcite}, \text{Anorthite}, \text{Kaolinite}\right\}.
\end{aligned}$$

Aqueous reactions are relatively fast and reach equilibrium instantaneously, so they can be represented by equilibrium reactions. Consequently, each aqueous reaction leads to a mass action law written as an algebraic relation that links the activities of the species involved in the reaction

$$a_l^j \;=\; K_j(T) \prod_{i \in I_p} \left(a_l^i\right)^{\nu_{ji}}, \quad j \in I_{sm} \cup I_{si}, \tag{2}$$

where a_l^j is the activity of component j in the liquid phase and ν_{ji} is the stoichiometric coefficient of the reaction. $K_j(T)$ is the reaction constant of component j that depends on the temperature T. Concerning gaseous species, activities are often replaced by fugacities

$$a_g^j \;=\; \varphi_g^j \, \frac{P_g^j}{P_0}, \tag{3}$$

where φ_g^j represents the fugacity coefficient of component j in the gaseous phase, P_g^j is the partial pressure of component j and P_0 is the atmospheric pressure.

Equilibrium reactions can take a different form for mineral precipitation or dissolution processes. In this case, a solubility product has to be verified:

$$\text{if } \; K_j(T) \prod_{i \in I_p} \left(a_\alpha^i\right)^{\nu_{ji}} < 1 \text{ then } c_s^j \;=\; 0, \text{else } K_j(T) \prod_{i \in I_p} \left(a_\alpha^i\right)^{\nu_{ji}} = 1 \;,\; j \in I_{se}. \tag{4}$$

Eq. 4 can be reformulated as a complementarity problem:

$$\min\left(c_s^j,\; 1 \;-\; K_j(T) \prod_{i \in I_p} \left(a_\alpha^i\right)^{\nu_{ji}}\right) \;=\; 0 \;,\; j \in I_{se}. \tag{5}$$

In contrast to equilibrium reactions, kinetic reactions are relatively slow, and in this paper, we consider that they only occur as mineral precipitation or dissolution. Reaction rates describe the mineral evolution over time. Each kinetic reaction leads to an ordinary differential equation written for the mineral reaction j [24]:

$$\frac{dc_s^j}{dt} \;=\; -\, r_j, \quad j \in I_{sk}, \tag{6}$$

where the reaction rate r_j is defined as

$$r_j \;=\; K_j^s(T)\, A_j^s \left(1 \;-\; K_j(T) \prod_{i \in I_p} \left(a_\alpha^i\right)^{\nu_{ji}}\right). \tag{7}$$

A_j^s is the reactive surface [$m^2.m^{-3}$] of component j, while K_j^s is the kinetic rate constant [$mol.m^{-2}.s^{-1}$] that depends on the temperature through the Arrhenius law [25, 43]

$$K_j^s(T) \;=\; K_{j,ref}\,\exp\left[-\frac{E_j^a}{R}\left(\frac{1}{T}-\frac{1}{298.15}\right)\right], \tag{8}$$

where $K_{j,ref}$, E_j^a, R and T are the reaction constants at a temperature of 298.15 K, activation energy [$J.mol^{-1}$], ideal gas constant [$J.K^{-1}.mol^{-1}$] and absolute temperature [K], respectively.

To describe the flow, we need to write a mass conservation law for each primary species present in each phase. We consider a direct substitutional approach (DSA) that consists of replacing concentrations of secondary species with a function depending on the concentrations of primary species using mass action laws

$$c_\alpha^j \;\stackrel{\text{def}}{=}\; \mathbb{C}_\alpha^j(\mathbf{c_p})\;,\; j \in I_{sm} \cup I_{si}, \tag{9}$$

where $\mathbf{c_p}$ is defined as a vector composed of primary species concentrations: $\mathbf{c_p} \;=\; \left(c_\alpha^i\right)\;, i \in I_p$. Using this formalism, mass conservation laws for primary species can be written as follows:

$$\begin{aligned}
&\frac{\partial}{\partial t}\left(\phi S_\alpha c_\alpha^i + \sum_{j\in I_{sm}} \phi \nu_{ji} S_\alpha \mathbb{C}_\alpha^j(\mathbf{c_p}) + \sum_{j\in I_s \setminus I_{sm}} \nu_{ji}\mathbb{C}_s^j(\mathbf{c_p})\right) + L_\alpha(c_\alpha^i) \\
&+ \sum_{j\in I_{sm}} \nu_{ji} L_\alpha(\mathbb{C}_\alpha^j(\mathbf{c_p})) \;=\; 0, \quad i \in I_{pm}, \qquad (10)\\
&\frac{\partial}{\partial t}\left(c_s^i + \sum_{j\in I_{si}} \nu_{ji}\mathbb{C}_s^j(\mathbf{c_p})\right) \;=\; 0, \quad i \in I_{pi}, \qquad (11)
\end{aligned}$$

where ϕ [-] stands for the porosity, S_α [-] for the saturation of the α phase and c_α^i [$mol.m^{-3}$] for the molar concentration of component i in phase α. For convenience, we also define L_α as the advection-diffusion operator in phase α

$$L_\alpha(c_\alpha^i) = \nabla\cdot(c_\alpha^i \vec{q}_\alpha) - \nabla\cdot(D_\alpha \nabla c_\alpha^i). \tag{12}$$

Using the approach of Millington and Quirk [27], the dispersive-diffusive tensor D_α [$m^2.s^{-1}$] is defined as

$$D_\alpha = \phi^{\frac{4}{3}} S_\alpha^{\frac{10}{3}} D_{m,\alpha}\mathbb{I} + d_L|\vec{q}_\alpha|\mathbb{I} + (d_L - d_T)\frac{\vec{q}_\alpha \vec{q}_\alpha{}^T}{|\vec{q}_\alpha|}, \tag{13}$$

where $D_{m,\alpha}$ [$m^2.s^{-1}$] is the molecular diffusion coefficient in phase α, and d_L [m] and d_T [m] are the amplitudes of longitudinal and transverse dispersion, respectively. $\vec{q}_\alpha$ [$m.s^{-1}$] is the velocity of phase α defined by the Darcy-Muskat equation

$$\vec{q}_\alpha \;=\; -\,\mathbb{K}\,\frac{k_{r\alpha}(S_\alpha)}{\mu_\alpha}\,(\nabla P_\alpha - \rho_\alpha^{mass}\vec{g})\,. \tag{14}$$

Here, $\mathbb{K}$ [m^2] is the absolute permeability tensor; $k_{r\alpha}$ [-] is the relative permeability of phase α; μ_α [Pa.s], P_α [Pa], and ρ_α^{mass} [$kg.m^{-3}$] are the dynamic viscosity, pressure and mass density of phase α, respectively; and $\vec{g}$ [$m.s^{-2}$] is the gravitational acceleration.

To take into account the effects of temperature, a conservation of energy is coupled to all the equations defined before

$$\frac{\partial}{\partial t}\left(\phi\sum_\alpha \rho_\alpha u_\alpha S_\alpha + (1-\phi)\rho_s c_h T\right) + \nabla.\left(-\lambda_{pm}\nabla T + \sum_\alpha \rho_\alpha h_\alpha \vec{q}_\alpha\right) \;=\; 0, \tag{15}$$

where T represents the absolute temperature [K]. This equation is divided into four parts: the first part defines a heat storage term with the internal energy $u_\alpha = h_\alpha - \dfrac{P_\alpha}{\rho_\alpha}$ [J.kg^{-1}], where h_α [J.kg^{-1}] is the enthalpy of phase α. The second part denotes the heat stored in the solid matrix and c_h [J.(kg.K)$^{-1}$] denotes the heat capacity of the rocks. The third part represents the heat conduction with λ_{pm} [W.m^{-1}.K^{-1}] as the thermal conductivity of the porous medium, and the last term characterizes the heat transport due to advection in the fluid phases.

To close the system, additional relations are added to fully characterize the problem. First, we add total restrictions on saturations and molar fractions

$$\sum_\alpha S_\alpha = 1 \quad \text{and} \quad \sum_i x_\alpha^i = 1. \tag{16}$$

Capillary pressure characterizes the pressure induced by interfacial tensions between each phase and is defined as

$$P_c(S_l) = P_g - P_l. \tag{17}$$

Finally, the global system is composed of a highly nonlinear system of $(N_p + 1)$ degenerate PDEs modeling the nonisothermal two-phase flow (N_p mass conservation laws (10)-(11) and one energy equation law (15)), coupled with card$\{I_{sm} \cup I_{si}\}$ algebraic equations (2), card$\{I_{se}\}$ complementary problems (5) and card$\{I_{sk}\}$ ODEs (6), subject to the boundary and initial conditions.

Let us end this section with the following remark. Thermophysical and geochemical properties such as fluid (gas and liquid) density and viscosity, and thermodynamic and kinetic data for mineral water gas reactions are calculated by equations of state as a function of temperature. In particular, the solubility of CO_2 and carbonate rocks is higher at lower temperatures. Consequently, the dissolution process is expected to be more important in cold regions due to low-temperature injection. Specifically in [38], two phenomena related to low-temperature injection were studied. On the one hand, exothermic CO_2 dissolution occurs, leading to a small increase in the temperature in the plume region. On the other hand, the Joule-Thompson effect creates a cooling effect of approximately 2°C on the temperature profile close to the injection well. This cooling is due to a thermodynamic process that can be related to the isenthalpic expansion of a real gas. Such temperature variations can result in more important changes in mineral precipitation or dissolution. Their conclusion highlights the fact that considering the nonisothermal process is important for obtaining accurate simulations focused on near well regions.

3 Resolution methods and numerical schemes

This section is devoted to presenting the two strategies used to solve THC processes in subsurface problems. On the one hand, the system can be solved in a fully implicit manner where all the equations are gathered in a large matrix. On the other hand, multiphase flow and reactive transport problems can be decoupled and solved sequentially. The fully coupled fully implicit and sequential approaches will be described as well as the FV discretization of the fully implicit scheme.

Using the strategy presented in [9], we first considered a fully coupled fully implicit resolution of the system of Eqs. (10)-(11)-(15)-(2)-(5)-(6). The DSA has the advantage of reducing the number of unknowns and thus easing the solution of the fully coupled problem. In return, the system to be solved is highly nonlinear, and the nonlinearity is further increased by the inclusion of thermal effects.

The sequential approach, also known as the operator splitting approach, decouples the problem into two subproblems and solves them separately and sequentially.

Our strategy is illustrated in Fig. 1. Specifically, using the sets of species defined in Sect. 2, our sequential strategy consists of initially solving a nonisothermal compositional two-phase flow. This first subproblem is composed of Eq. (10) for i $\in I_{2\varphi}$ in which, the contributions of the remaining species are

treated explicitly, as well as the energy balance equation (15). We assume that all the exchanges between the liquid and gas phases are computed in this step. Then, a reactive transport problem composed of Eqs. (10) and (11) for i $\in I_{rt}$ is solved to compute the concentration of the remaining species, using the quantities provided by the first subproblem (velocity, saturation, molar density, temperature, etc.). Each subproblem is solved implicitly using the DSA presented above. For more details, we refer to [8] where a similar strategy was considered to deal with isothermal reactive multiphase flows.

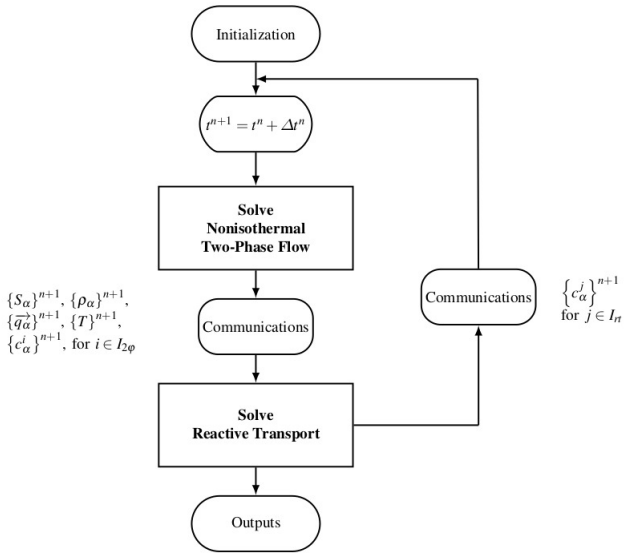

Figure 1: Sequential scheme of the proposed strategy

Here, we only describe the discretization of the fully coupled fully implicit scheme using a conservative FV method. More precisely, we use a cell-centered FV scheme that consists of integrating the equations of the problem on a control volume denoted by V_k, and evaluating the fluxes at the interface γ_{kl} between two neighboring volumes V_k and V_l. The time discretization is carried out with a second-order backward differentiation formula with a variable time step [31], to increase the efficiency and stability of the scheme. Using the following parameters,

$$\Delta t^n = t^{n+1} - t^n, \Delta t^{n-1} = t^n - t^{n-1},$$
$$\beta_1 = \frac{1}{\Delta t^n}\left(1 + \frac{\Delta t^n}{\Delta t^n + \Delta t^{n-1}}\right), \beta_{-1} = \frac{1}{\Delta t^{n-1}}\left(\frac{\Delta t^n}{\Delta t^n + \Delta t^{n-1}}\right), \beta_0 = -(\beta_1 + \beta_{-1}),$$

the discretization of the set of Eqs. (10)-(11)-(15)-(2)-(5)-(6) on a control volume V_k is given by

$$
\begin{aligned}
&\frac{|V_k|}{\Delta t^n}\left(\beta_1\left\{\phi S_\alpha c_\alpha^i\right\}_k^{n+1}+\beta_0\left\{\phi S_\alpha c_\alpha^i\right\}_k^{n}+\beta_{-1}\left\{\phi S_\alpha c_\alpha^i\right\}_k^{n-1}\right)\\
&+\sum_{j\in I_{sm}} \nu_{ji}\frac{|V_k|}{\Delta t^n}\left(\beta_1\left\{\phi S_\alpha \mathbb{C}_\alpha^j(\mathbf{c_p})\right\}_k^{n+1}+\beta_0\left\{\phi S_\alpha \mathbb{C}_\alpha^j(\mathbf{c_p})\right\}_k^{n}+\beta_{-1}\left\{\phi S_\alpha \mathbb{C}_\alpha^j(\mathbf{c_p})\right\}_k^{n-1}\right)\\
&+\sum_{j\in I_s\setminus I_{sm}} \nu_{ji}\frac{|V_k|}{\Delta t^n}\left(\beta_1\left\{\mathbb{C}_s^j(\mathbf{c_p})\right\}_k^{n+1}+\beta_0\left\{\mathbb{C}_s^j(\mathbf{c_p})\right\}_k^{n}+\beta_{-1}\left\{\mathbb{C}_s^j(\mathbf{c_p})\right\}_k^{n-1}\right)\\
&+\sum_{l|V_k\cap V_l\neq\emptyset}|\gamma_{kl}|\left(\left\{c_\alpha^i\right\}_{kl}^{n+1}\left\{\vec{q}_\alpha\right\}_{kl}^{n+1}-\left\{D_\alpha\right\}_{kl}^{n+1,har}\left\{\nabla c_\alpha^i\right\}_{kl}^{n+1}\right)\cdot\vec{n}_{kl}\\
&+\sum_{j\in I_{sm}}\nu_{ji}\sum_{l|V_k\cap V_l\neq\emptyset}|\gamma_{kl}|\left(\left\{\mathbb{C}_\alpha^j(\mathbf{c_p})\right\}_{kl}^{n+1}\left\{\vec{q}_\alpha\right\}_{kl}^{n+1}-\left\{D_\alpha\right\}_{kl}^{n+1,har}\left\{\nabla\mathbb{C}_\alpha^j(\mathbf{c_p})\right\}_{kl}^{n+1}\right)\cdot\vec{n}_{kl}=0\,,\ i\in I_{pm},
\end{aligned}
\tag{18}
$$

$$
\begin{aligned}
&\frac{|V_k|}{\Delta t^n}\left(\beta_1\left\{c_s^i\right\}_k^{n+1}+\beta_0\left\{c_s^i\right\}_k^{n}+\beta_{-1}\left\{c_s^i\right\}_k^{n-1}\right)\\
&+\sum_{j\in I_{si}}\nu_{ji}\frac{|V_k|}{\Delta t^n}\left(\beta_1\left\{\mathbb{C}_s^j(\mathbf{c_p})\right\}_k^{n+1}+\beta_0\left\{\mathbb{C}_s^j(\mathbf{c_p})\right\}_k^{n}+\beta_{-1}\left\{\mathbb{C}_s^j(\mathbf{c_p})\right\}_k^{n-1}\right)=0\,,\ i\in I_{pi},
\end{aligned}
\tag{19}
$$

$$
\begin{aligned}
&\frac{|V_k|}{\Delta t^n}\left(\beta_1\sum_\alpha\left\{\phi\rho_\alpha u_\alpha S_\alpha\right\}_k^{n+1}+\beta_0\sum_\alpha\left\{\phi\rho_\alpha u_\alpha S_\alpha\right\}_k^{n}+\beta_{-1}\sum_\alpha\left\{\phi\rho_\alpha u_\alpha S_\alpha\right\}_k^{n-1}\right)\\
&+\frac{|V_k|}{\Delta t^n}\left(\beta_1\left\{(1-\phi)\rho_s c_h T\right\}_k^{n+1}+\beta_0\left\{(1-\phi)\rho_s c_h T\right\}_k^{n}+\beta_{-1}\left\{(1-\phi)\rho_s c_h T\right\}_k^{n-1}\right)\\
&+\sum_{l|V_k\cap V_l\neq\emptyset}|\gamma_{kl}|\left(-\left\{\lambda_{pm}\right\}_{kl}^{n+1,har}\left\{\nabla T\right\}_{kl}^{n+1}+\sum_\alpha\left\{\rho_\alpha h_\alpha\right\}_{kl}^{n+1}\left\{\vec{q}_\alpha\right\}_{kl}^{n+1}\right)\cdot\vec{n}_{kl}=0\,,
\end{aligned}
\tag{20}
$$

$$
\min\left(\left\{c_s^j\right\}_k^{n+1},\ 1-K_j(T^{n+1})\prod_{i\in I_p}\left\{\left(a_\alpha^i\right)^{\nu_{ji}}\right\}_k^{n+1}\right)=0\,,\ j\in I_{se},
\tag{21}
$$

$$
\left\{c_s^j\right\}_k^{n+1}=\left\{c_s^j\right\}_k^{n}-\Delta t^n K_j^s(T^{n+1})A_j^s\left(1-K_j(T^{n+1})\prod_{i\in I_p}\left\{(a_\alpha^i)^{\nu_{ji}}\right\}_k^{n+1}\right),\ j\in I_{sk}.
\tag{22}
$$

$\vec{n}_{kl}$ is the unit outer normal to the interface γ_{kl}, and $V(k)$ denotes the set of adjacent elements of V_k. Finally, the Darcy-Muskat velocity is discretized as follows

$$
\left\{\vec{q}_\alpha\right\}_{kl}^{n+1}=-\left\{\mathbb{K}\right\}_{kl}^{har}\left\{\frac{k_{r\alpha}(S_\alpha)}{\mu_\alpha}\right\}_{kl}^{n+1,up}\left(\left\{\nabla P_\alpha\right\}_{kl}^{n+1}-\left\{\rho_\alpha^{mass}\right\}_{kl}^{n+1,ari}\vec{g}\right).
$$

The convective flux terms are approximated by using an upwind scheme; thus, unknown quantities (S_α, P_α, c_α^i, $k_{r\alpha}$ and h_α) are evaluated implicitly and upstream at the interface γ_{kl} with

$$
\{\cdot\}_{kl}^{n+1,up}=\begin{cases}\{\cdot\}_k^{n+1} & \text{if}\quad \{\vec{q}_\alpha\}_{kl}^{n+1}\cdot\vec{n}_{kl}>0,\\ \{\cdot\}_l^{n+1} & \text{else.}\end{cases}\quad\text{and}\ \{\cdot\}_k^{n+1}=\frac{1}{|V_k|}\int_{V_k}\{\cdot\}^{n+1}dV.
$$

The discrete gradients are computed by using either the TPFA or MPFA (see, e.g., [18, 6]) depending on the complexity of the mesh. In this study, we used only the TPFA scheme. More details about its implementation and the expression of transmissibilities can be found in [2]. Different average methods are used to calculate some quantities between two neighboring elements; for example, a harmonic average is used for $\{\mathbb{K}\}_{kl}^{har}$, $\{D_\alpha\}_{kl}^{n+1,har}$, $\left\{\lambda_{pm}\right\}_{kl}^{har}$ and an arithmetic average is used for $\{\rho_\alpha^{mass}\}_{kl}^{n+1,ari}$. The boundary and initial conditions complete the FV discretization of the system (18)-(22). This leads to a set of strongly nonlinear equations.

The next section is dedicated to the numerical implementation of our fully implicit and sequential strategies in the DuMu^X simulation platform and its validation through two CO_2 storage scenarios.

4 Numerical simulation

In this section, we present the numerical results for test cases modeling different scenarios of THC processes for CO_2 storage in saline aquifers. In Subsection 4.1, we briefly present the implementation based on the DuMu^X platform for the two modules developed to simulate THC processes. Then, to validate our strategy, we present two test cases involving nonisothermal two-phase flow coupled with reactive transport. First in Subsection 4.2, our approach is validated by solving a one-dimensional radial test case. Then, this work is extended to two- and three-dimensional cases to increase the complexity and to check the competitiveness of the code on large problems with grids involving millions of unknowns where the use of high-performance computing becomes crucial. The two-dimensional results are not presented in this work since the conclusions are similar to those drawn from the one-dimensional case. Instead, we prefer to focus on a realistic three-dimensional test problem. Consequently, Subsection 4.3 presents our numerical results for the benchmark problem based on the Johansen CO_2 storage operation [16]. All test cases show that our strategies are suitable to simulate coupled nonisothermal multiphase flow and reactive transport problems. To ensure the reproducibility of the results of the two presented tests, all necessary data, including discretization and solvers, are specified.

4.1 Implementation

All the numerical developments have been implemented in the DuMu^X platform, which is an open-source code. It provides many numerical tools to solve PDEs mainly related to porous media, but also allows, mesh management, discretization or linear and nonlinear solvers. DuMu^X, based on the Distributed and Unified Numerics Environment (DUNE) [12], has been written in C++ to benefit from the power provided by object-oriented languages. Concerning the numerical strategy, we have developed two different modules aimed at solving THC processes for the CO_2 storage model, including the fully implicit and sequential approaches previously described. The modularity of DuMu^X facilitates the implementation of both approaches in the same numerical environment. Here, we choose to use a cell-centiered FV approach for spatial discretization. The time discretization has been upgraded from a first-order implicit Euler scheme to a second-order method to improve the accuracy of our scheme. Specifically, we have used a second-order backward differentiation formula (BDF2) as presented in Eqs. (18)-(22). The resulting coupled nonlinear equations are solved using a Newton-Raphson algorithm with numerically computed Jacobian matrices. An adaptive time stepping method based on the number of iterations required by the Newton-Raphson method to reach convergence is employed. The time step is reduced if the number of iterations is less than a target number and increased otherwise. The linearized systems of equations are solved by a preconditioned iterative linear solver. Specifically, a biconjugate gradient stabilized (BiCGSTAB) method [11] with an algebraic multigrid (AMG) preconditioner [13] is used. Thanks to the DUNE parallel library, the DuMu^X simulation platform supports

parallel computations using a distributed memory model based on message passing interface (MPI) communications. This enables heavy calculations relevant to large-scale field applications.

4.2 Test 1: One-dimensional radial problem

The first test addresses a one-dimensional problem that allows studying thermal effects on injectivity during CO_2 storage. First, we present a numerical convergence study for different quantities of interest followed by a comparison between isothermal and nonisothermal results.

4.2.1 Test 1 case configuration

The first test case deals with a one-dimensional radial problem initially proposed by [45]. This test addresses a THMC model for CO_2 geological sequestration. Here we focus only on THC processes and we neglect the mechanical effects. A homogeneous reservoir 10 km long and 100 m high is considered. A schematic diagram of the domain is shown in Fig. 2. The injection is set up with a well located at the left part of the domain at a rate of 90 kg.s^{-1} over 10 years. The initial temperature of the reservoir is fixed at 348.15 K, whereas the injection temperature is cooler at 305.15 K to inject CO_2 in its supercritical phase. Low-temperature injection is supposed to dissolve more supercritical CO_2 into the aqueous phase, which can enhance the solubility trapping of supercritical CO_2 and prevent damage close to the injection area. All the physical data can be found in Table 2. The initial time step is set to 10^{-5} s, and the maximum time step is set to 10^6 s. The tolerances for the Newton-Raphson and BICGSTAB methods are 10^{-6} and 10^{-8}, respectively. In this case, the Newton-Raphson method converges rapidly in fewer than 5 iterations on average.

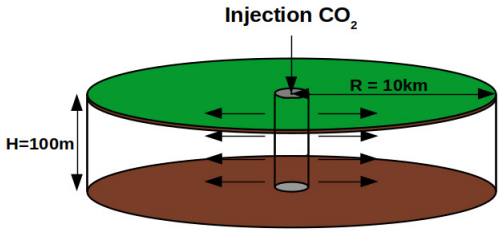

Figure 2: Schematic diagram of the one-dimensional test case proposed in [45]

In [45], the authors considered three different runs of increasing complexity with different initial compositions. In this work, we focused on the second run dealing with the eight chemical reactions detailed in Table 3. The first reaction expresses gaseous CO_2 dissolution into the liquid phase at the equilibrium state. Once CO_2 is dissolved in the liquid phase, it reacts with the resident H_2O to form bicarbonate HCO_3^- and hydrogen H^+ ions. These two ions will then initiate other reactions. Consequently, we can account for six aqueous complexation reactions that we consider at equilibrium. The last chemical reaction describes a precipitation/dissolution reaction involving solid calcite that is also considered at equilibrium. We consider that calcite initially represents a volume fraction (VF) of 5% of the rock and that the remaining 95% of the rock is inert.

Finally, thanks to the Morel formalism, we have chosen to split species into primary and secondary species as follows:

$$I_p = \left\{H_2O_{(l)},\, CO_{2(l)},\, H^+,\, Ca^{2+}\right\},$$
$$I_s = \left\{CO_{2(g)}, OH^-,\, CO_3^{2-},\, HCO_3^-,\, CaCO_{3(l)},\, CaHCO_3^+,\, CaOH^+,\, CaCO_{3(s)}\right\}.$$

Table 2: Simulation data of the one-dimensional test case proposed in [45]

Constitutive law or variable	Symbol	Parameters	Unit
Formation radius	R	10000	[m]
Formation height	H	100	[m]
Porosity	ϕ	0.3	[-]
Permeability	$\mathbb{K}$	10^{-13}	[m^2]
Initial Pressure	P_{init}	2×10^7	[Pa]
Initial Temperature	T_{init}	348.15	[K]
Injection Temperature	T_{inj}	305.15	[K]
Injection Rate	Q_{inj}	90	[$kg.s^{-1}$]
Van Genuchten parameter	α	5.1×10^{-5}	[Pa^{-1}]
Van Genuchten parameter	m	0.457	[-]
Residual liquid saturation	S_{lr}	0.3	[-]
Residual gaseous saturation	S_{gr}	0.05	[-]
Solid Density	ρ_s	2000	[$kg.m^{-3}$]
Solid Thermal Conductivity	λ_s	2.5	[$W.(m.K)^{-1}$]
Solid Heat Capacity	c_h	1000	[$J.(kg.K)^{-1}$]
Longitudinal Dispersion	d_L	0	[m]
Transverse Dispersion	d_T	0	[m]
Liquid molecular diffusion	D_l	0	[$m^2.s^{-1}$]
Gaseous molecular diffusion	D_g	0	[$m^2.s^{-1}$]

Table 3: Chemical reactions involved in the one-dimensional test case proposed in [45]

Reactions		
$CO_{2(g)}$	$\rightleftharpoons$	$CO_{2(l)}$
$OH^- + H^+$	$\rightleftharpoons$	$H_2O_{(l)}$
$CO_3^{2-} + H^+$	$\rightleftharpoons$	HCO_3^-
$CO_{2(l)} + H_2O_{(l)}$	$\rightleftharpoons$	$H^+ + HCO_3^-$
$CaCO_{3(l)} + H^+$	$\rightleftharpoons$	$Ca^{2+} + HCO_3^-$
$CaHCO_3^+$	$\rightleftharpoons$	$Ca^{2+} + HCO_3^-$
$CaOH^+ + H^+$	$\rightleftharpoons$	$Ca^{2+} + H_2O_{(l)}$
$CaCO_{3(s)} + H^+$	$\rightleftharpoons$	$Ca^{2+} + HCO_3^-$

Table 4: Initial conditions for primary species

Primary species	Initial molality [$mol.kg^{-1}$]
$CO_{2(l)}$	3.67×10^{-7}
H^+	7.51×10^{-9}
Ca^{2+}	2.38×10^{-5}

The initial molalities of the primary species have been recalculated at equilibrium by a flash calculation and are given in Table 4. For this calculation, we used geochemistry data available in the Chess thermodynamic database [1] as input.

4.2.2 Numerical results

First, to validate our implementation, we conducted a numerical convergence study by using several structured meshes composed of 2000, 1000, 500, 250 and 125 cells, leading to cells ranging from 5 m to 80 m. The computations for this test case were all performed using the fully coupled fully implicit approach presented in Sect. 3.

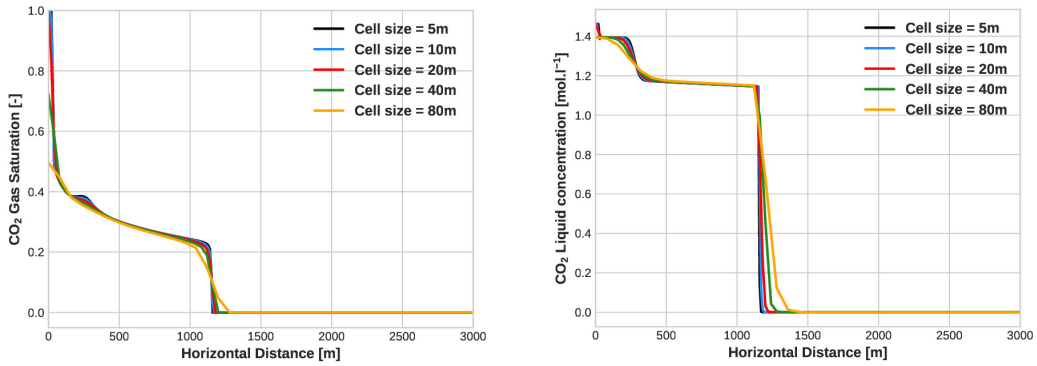

(a) Saturation of the gaseous phase

(b) $CO_{2(l)}$ concentration

Figure 3: Mesh convergence for the saturation of the gaseous phase (a) and $CO_{2(l)}$ concentration (b) at 10 years

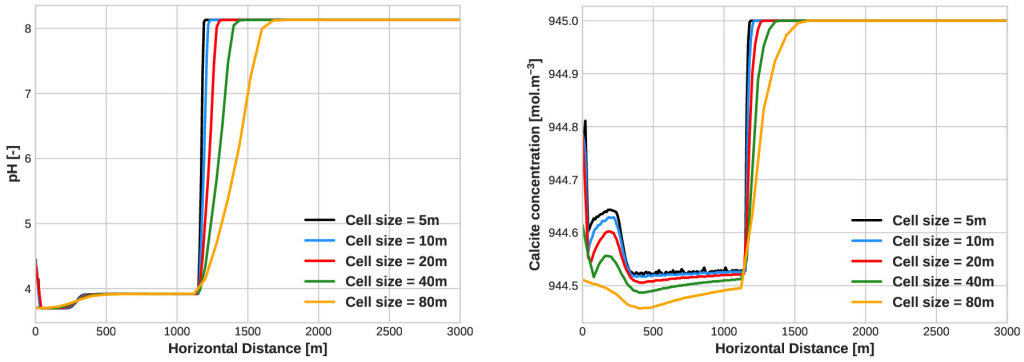

(a) pH

(b) Calcite concentration

Figure 4: Mesh convergence for the pH (a) and calcite concentration (b) at 10 years

The saturation profile (Fig. 3 (a)) indicates that gaseous CO_2 fully saturates the near-well part of the domain. This phenomenon clearly depends on the mesh size since it is not observed for large cell sizes. However, the gaseous front of CO_2 can be located 1200 meters from the injection well. This gaseous CO_2 tends to dissolve into the resident brine, initially saturating the porous medium, which results in an increase in the liquid CO_2 concentration in the plume region of Fig. 3 (b). The saturation and concentration fronts are very sharp, as remarkably captured by the simulation. The injected CO_2 reacts with the brine to release H^+ ions, as observed with the decrease in pH in Fig. 4 (a). Moreover,

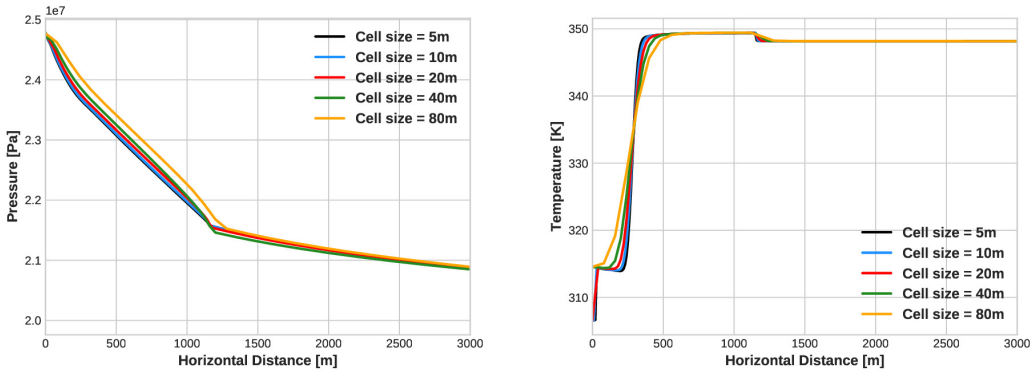

(a) Pressure of the gaseous phase

(b) Temperature

Figure 5: Mesh convergence for the pressure of the gaseous phase (a) and temperature (b) at 10 years

these ions also activate the precipitation/dissolution reaction of calcite. Here, calcite is considered to be initially at equilibrium, and its dissolution only occurs in the CO_2 plume region (Fig. 4 (b)). The temperature is modified only in the near-well region. In fact, the heat transfer (Fig. 5 (b)) seems to be driven by conduction more than by convection. Consequently, only the near-well region is cooled due to low-temperature injection.

A mesh convergence analysis for several quantities is also presented in Fig. 6. It represents the L^2-relative error between several variables and the reference solution (computed with the mesh composed of 2000 elements) as a function of the mesh size on the entire domain at $t = 10$ years. The discretization schemes are essentially first-order schemes in space, which explains an order of convergence close to 1. The convergence of some quantities is degraded due to the complexity of the phenomena considered and their strong nonlinearity. We note that for the three-dimensional mesh used in the next section, this convergence analysis for the TPFA scheme has not been performed. Indeed, despite an unchallenging mesh, the K-orthogonality property is not perfectly ensured, even if the results obtained by TFPA and nonlinear TFPA in [34] differed only slightly.

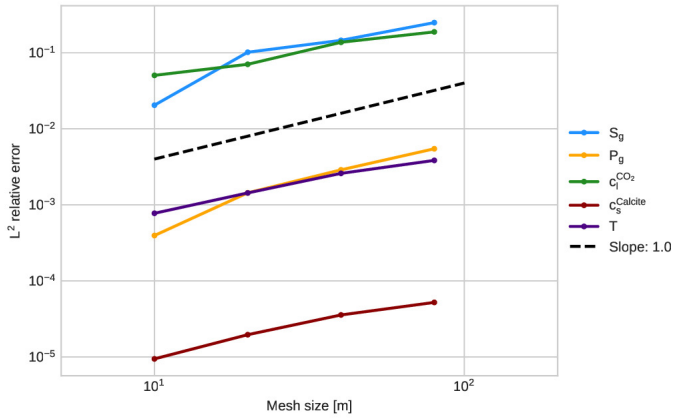

Figure 6: L^2-relative error for $CO_{2(l)}$ concentration, gas saturation, gas pressure, temperature and calcite concentration as a function of cell size

4.2.3 Comparison between isothermal and nonisothermal processes

To highlight the effects of temperature, a comparison between isothermal and nonisothermal test cases was carried out. This comparison has been established on the same test case, with exactly the same data. The only difference comes from the fact that the isothermal case was performed with an injection temperature equal to the temperature of the reservoir. Figs. 7, 8 and 9 represent the evolution of several quantities at 1, 3, 5 and 10 years for both isothermal and nonisothermal scenarios.

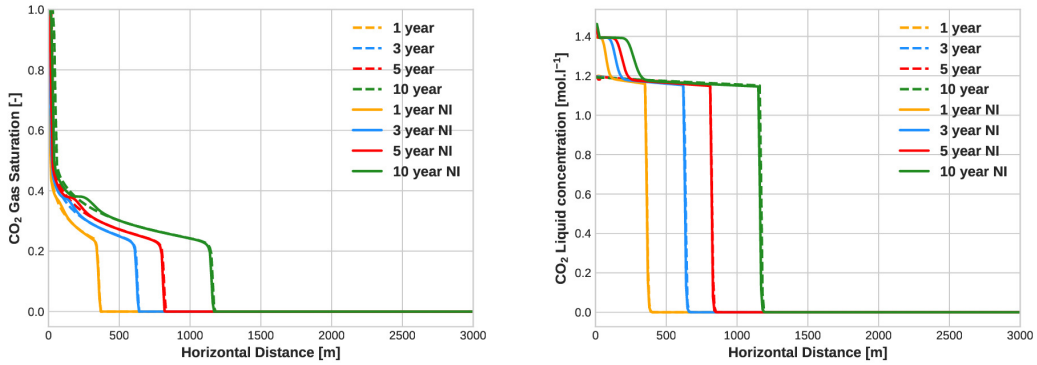

(a) Saturation of gaseous phase (b) Concentration of liquid CO_2

Figure 7: Evolution of the concentration of liquid CO_2 (a) and saturation of the gaseous phase (b). NI refers to the nonisothermal test case and the dashed line refers to the isothermal case

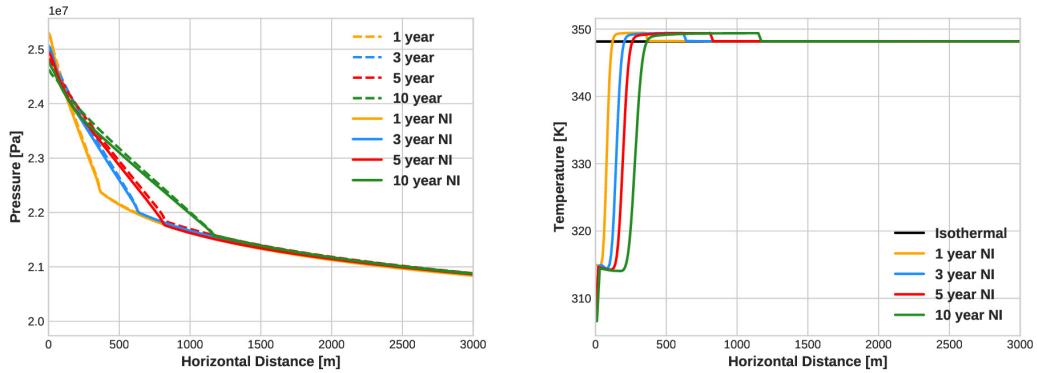

(a) Pressure of gaseous phase (b) Temperature

Figure 8: Evolution of gaseous phase pressure (a) and temperature (b)

As observed in [45], the front of the gas phase in Fig.7 (a) is located at the same distance from the injection well even if the viscosity of the fluid is impacted in the nonisothermal case. CO_2 dissolution only occurs where CO_2 and H_2O coexist. Figure 7 (b) depicts the concentration of liquid CO_2 and highlights a significant difference between the two cases. A 14% increase in dissolved CO_2 is observed near the injection well in the nonisothermal configuration. Figure 8 (b) shows that temperature profiles are significantly impacted only close to the well region (up to 250 m). A slight decrease between 0 and

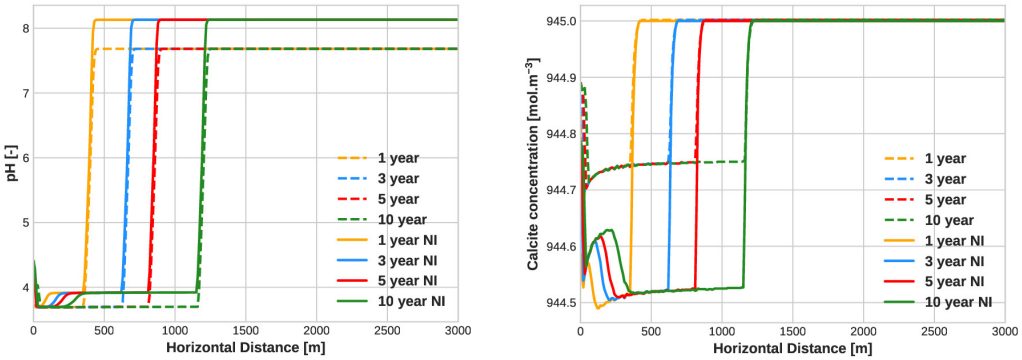

(a) pH (b) Calcite concentration

Figure 9: Evolution of pH (a) and calcite concentration (b)

250 m can be observed due to the Joule-Thompson effect. The temperature decreases because of the expansion of gaseous CO_2. In the same figure, it is possible to notice an increase in the temperature at the front of the plume of CO_2 expanding over time. This phenomenon is caused by CO_2 dissolution, which is an exothermic process. The pH and the evolution of the calcite concentration are represented in Figs. 9 (a) and (b). In both cases, low-temperature injection significantly affects the chemical processes and in particular increases the dissolution of calcite.

We conclude by noting that the general trends of the system behavior are in good agreement with the results obtained by [45]. More precisely, we observe the same variations between the isothermal and nonisothermal simulations as those observed in [45]. Variations in pH and calcite concentration seem to be sensitive to temperature as well as the concentration of liquid CO_2, which increases significantly for low-temperature injection. Therefore, the same conclusion can be drawn as in [45] on the thermal effects that have an important impact on the chemical process. As expected, low-temperature injection enhances the dissolution of supercritical CO_2 and solubility trapping.

4.3 Test 2: Three-dimensional heterogeneous medium

The second test is based on a benchmark initially studied by [16]. It is worth noting that most of the participants in the benchmark provided isothermal results on several industrial reservoir simulators or academic simulation platforms. First, we present some numerical results that illustrate the evolution of CO_2 for different quantities of interest after a period of 50 years. We also provide a comparison between the fully implicit and sequential results. Finally, we compare the performance, in terms of the computation time, and the parallel scalability of sequential and implicit methods.

4.3.1 Test 2 configuration

The Lower Jurassic Johansen Formation is a sandstone reservoir located in the northern North Sea. It has been studied and considered a reservoir candidate for CO_2 storage by Norwegian authorities. The mesh considered in this benchmark is a simplified structured geometry composed of the same material properties as the real Johansen model [5]. Figure 10 depicts the three- dimensional geometry, as well as the heterogeneous permeability of the domain. Porosity and other grid information are given together with the mesh format and, stored in the corner-point grid. To read such a grid, the ”opm-grid” module from the Open Porous Media [4] initiative is used, which supports the standard corner-point grid

format. The lateral extension of the domain is approximately 9600×8900 m and the vertical extension is composed of 9 layers of grid blocks in height. The injection well is located at $x = 5440$ m and $y = 3300$ m. The pressure of the liquid phase is hydrostatic and gravity- and height-dependent. Initially, a pressure of 2.53×10^7 Pa is set at 2500 m depth.

The simulation is conducted over a 25-year period of CO_2 injection at 15 kg.s^{-1} in the formation, followed by a 25-year period of postinjection during which the well is shut down. Simulation data are listed in Table 5. The initial time step is set to 10^{-2} s and the maximum time step is set to 10^7 s. The tolerances for the Newton-Raphson and BICGSTAB methods are 5×10^{-6} and 10^{-8}, respectively.

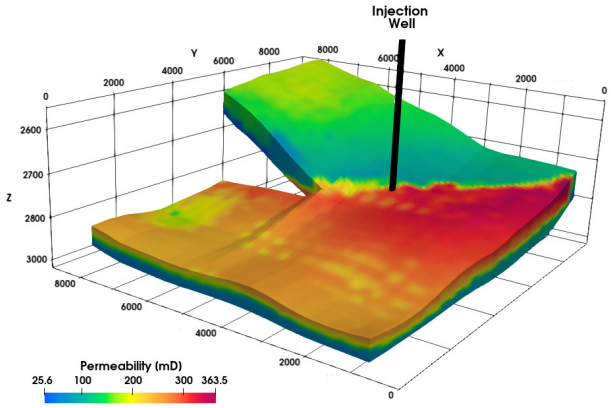

Figure 10: Permeability field for the Johansen grid geometry

Table 5: Simulation data for the three-dimensional heterogeneous test case from [16]

Constitutive law or variable	Symbol	Parameters	Unit
Initial Temperature	T_{init}	373.15	[K]
Injection Temperature	T_{inj}	323.15	[K]
Injection Rate	Q_{inj}	15	[kg.s^{-1}]
Residual liquid saturation	S_{lr}	0.2	[-]
Residual gaseous saturation	S_{gr}	0.05	[-]
Brooks Corey parameter	P_e	1×10^4	[Pa^{-1}]
Brooks Corey parameter	λ	2.0	[-]
Solid Density	ρ_s	2500	[kg.m^{-3}]
Solid Thermal Conductivity	λ_s	2.5	[W.(m.K)$^{-1}$]
Solid Heat Capacity	c_h	1000	[J.(kg.K)$^{-1}$]
Longitudinal Dispersion	d_L	0	[m]
Transverse Dispersion	d_T	0	[m]
Liquid molecular diffusion	D_l	2×10^{-9}	[m^2.s^{-1}]
Gaseous molecular diffusion	D_g	Based on [42]	[m^2.s^{-1}]

The chemical system considered in this test case is inspired by [19]. It is composed of seven reactions, one aqueous dissolution, three aqueous complexation reactions at equilibrium and three precipitation/dissolution reactions solved as kinetic reactions. All information concerning equilibrium constants, reactive constants, reactive surfaces and activation energies are given in Tables 6 and 7.

Thanks to the Morel formalism [28], chemical species are split into

Table 6: Chemical reactions involved in the three-dimensional heterogeneous test case from [19]

Reactions		
$CO_{2(g)}$	$\rightleftharpoons$	$CO_{2(l)}$
$OH^- + H^+$	$\rightleftharpoons$	$H_2O_{(l)}$
$CO_3^{2-} + 2\,H^+$	$\rightleftharpoons$	$H_2O_{(l)} + CO_{2(l)}$
$CO_{2(l)} + H_2O_{(l)}$	$\rightleftharpoons$	$H^+ + HCO_3^-$
Anorthite $+ 8\,H^+$	$\rightleftharpoons$	$4\,H_2O_{(l)} + Ca^{2+} + 2\,Al^{3+} + 2\,SiO_2$
Calcite $+ 2\,H^+$	$\rightleftharpoons$	$Ca^{2+} + H_2O_{(l)} + CO_{2(l)}$
Kaolinite $+ 6\,H^+$	$\rightleftharpoons$	$5\,H_2O_{(l)} + 2\,Al^{3+} + 2\,SiO_2$

Table 7: Chemical information about mineral species involved in kinetic reactions

Mineral	$\log_{10}(K_{j,ref})$	E^a	A_s [$m^2.m^{-3}$]	Init. conc. [$mol.m^-3$]
Anorthite	-12.0	67.830	88.0	87
Calcite	-8.8	41.870	88.0	238
Kaolinite	-13.0	62.760	17600	88

- for the fully implicit approach

$$
\begin{aligned}
I_{pm} &= \left\{H_2O_{(l)}, CO_{2(l)}, H^+, Ca^{2+}, Al^{3+}, SiO_2\right\},\\
I_{sm} &= \left\{H_2O_{(g)}, CO_{2(g)}, OH^-, CO_3^{2-}, HCO_3^-\right\},\\
I_{sk} &= \left\{\text{Anorthite}, \text{Calcite}, \text{Kaolinite}\right\},
\end{aligned}
$$

- for the sequential approach

$$
\begin{aligned}
I_{2\varphi} &= \left\{H_2O_{(l)}, H_2O_{(g)}, CO_{2(l)}, CO_{2(g)}\right\},\\
I_{rt} &= \left\{H^+, Ca^{2+}, Al^{3+}, SiO_2, OH^-, {CO_3}^{2-}, {HCO_3}^-, \text{Calcite}, \text{Anorthite}, \text{Kaolinite}\right\}.
\end{aligned}
$$

The initial mineral concentrations are given in Table 7, while Table 8 provides the initial conditions for each primary species. To close the problem, we set impermeable Neumann boundary conditions on the top and bottom boundaries of the domain, whereas Dirichlet conditions are fixed to initial values on lateral boundaries for pressure and concentrations.

Table 8: Initial conditions for primary species

Primary species	Initial molality [$mol.kg^{-1}$]
$CO_{2(l)}$	3.55×10^{-3}
H^+	5.71×10^{-1}
Ca^{2+}	2.52×10^{-2}
Al^{3+}	3.13×10^{-12}
SiO_2	4.73×10^{-4}

4.3.2 Numerical results

Computations were first performed with the fully coupled fully implicit scheme. Figure 11 shows the results for different quantities of interest. As CO_2 is injected at the bottom of the saline aquifer, it tends

to move upward and spread laterally once the plume reaches the top of the aquifer. This phenomenon is due to the density difference between gaseous CO_2 and the resident brine that fully saturates the domain at the beginning. The gaseous saturation depicts that the CO_2 injected at the boundary between two levels of heterogeneity tends to move preferentially in the lower permeability zone, but also in the shallower part of the aquifer. The temperature effects are also visible in Fig. 11 due to an injection at 50 K lower than the initial temperature of the reservoir. The temperature changes are localized at most over three to four cells around the injection well, which is consistent with what has been observed in the one-dimensional radial test case presented previously. The minimum temperature of 340 K is reached at the end of the injection scenario at 25 years, and then the heat conduction of the host rock tends to warm the cooled region step by step. Moreover, the pH is modified in the CO_2 plume region as well as the calcite. When CO_2 is transformed from the gaseous to liquid phase due to reservoir conditions, it reacts with the resident brine, releasing hydrogen and bicarbonate ions. A pH decrease means that more hydrogen ions H^+ are released than hydroxide ions OH^-. This tends to activate mineral reactions of precipitation or dissolution over large time scales. In this case, the dissolution of calcite can be observed in the same zone. The calcite concentration has decreased by approximatively 0.5 $mol.m^{-3}$ in the region where CO_2 is located.

Our results are close to those presented in Fig. 12 obtained using the open source GEOS simulator [3].

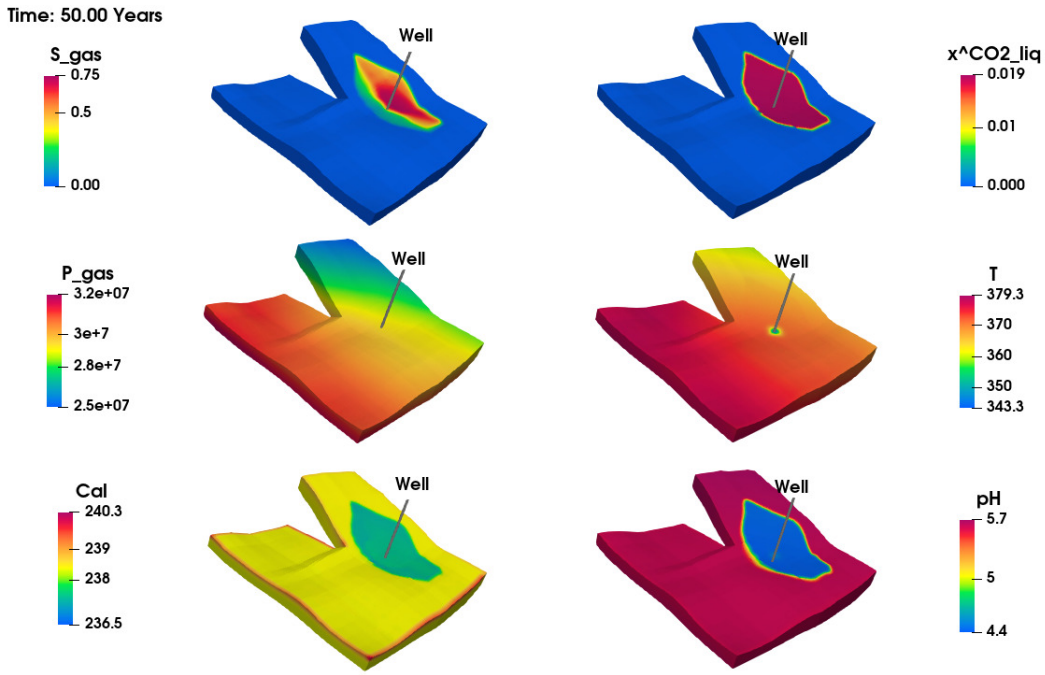

Figure 11: Simulation results for the fully implicit approach at $t = 50$ years

4.3.3 Comparison between fully implicit and sequential approaches

Figure 13 shows a comparison of several quantities between the fully implicit and sequential methods. A small difference is noticeable in the shape of the CO_2 plume. In terms of construction, the sequential scheme is not fully conservative. Splitting errors are mainly due to the explicit treatment of data between the two subproblems. The fully implicit scheme is more accurate, but more complicated to solve

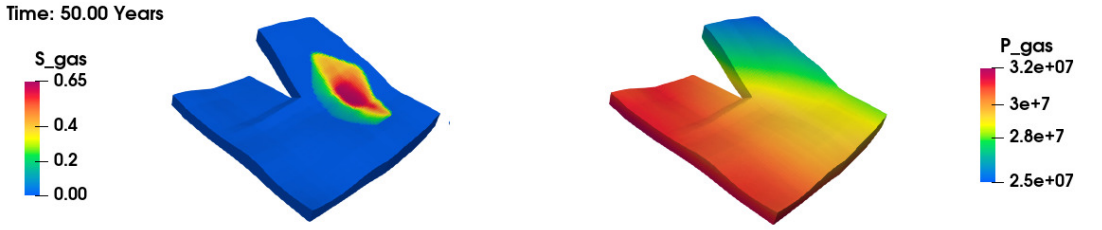

Figure 12: Simulation results obtained by GEOS at $t = 50$ years

numerically. Table 9 shows the relative difference in the L^2-norm over the entire domain between the sequential and fully implicit solutions at $t = 50$ years. The difference decreases when the maximum time step is reduced.

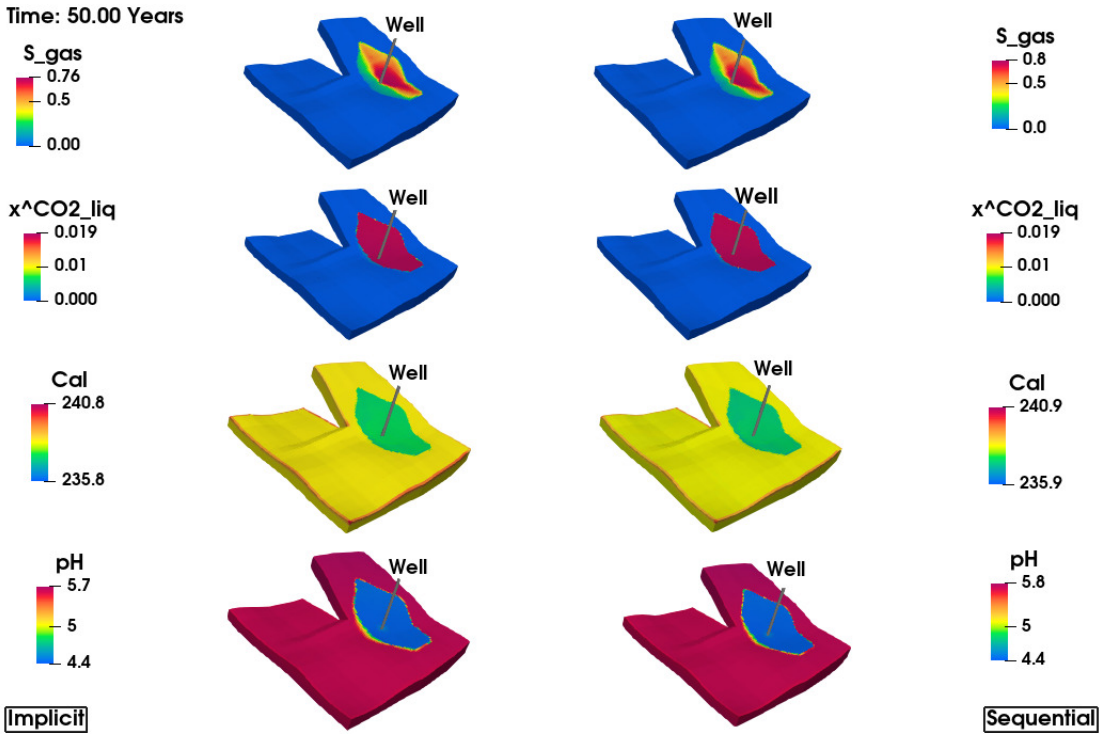

Figure 13: Comparison of the solutions between the fully implicit and sequential schemes at $t = 50$ years

Figure 14 represents the amount of CO_2 in the gas phase, dissolved in the liquid phase and converted into calcite within the model domain as a function of time for both strategies. The distribution of CO_2 in the liquid and gas phases is very close to the results obtained with the GEOS and ECLIPSE simulators (as shown in Fig. 14) as well as other simulators used by participants in [16]. During the injection step, the gaseous saturation increases before slightly decreasing due to the dissolution of CO_2 in the liquid phase in the postinjection period. Solubility trapping is indeed a process with a significant impact on the efficiency of storage. However, mineral trapping is not very efficient on short time scales, and therefore, the CO_2 turned into calcite increases very slowly until 50 years. Nevertheless, mineral trapping is

Table 9: Relative difference in L^2-norm between several quantities computed by the fully implicit and sequential approaches on 54756 cells at $t = 50$ years

dt_{max}	S_g	P_g	$x_l^{CO_2}$	Calcite	pH
5×10^6	1.52×10^{-2}	7.41×10^{-5}	3.29×10^{-2}	1.0×10^{-4}	1.90×10^{-2}
2×10^6	9.13×10^{-3}	4.00×10^{-6}	2.10×10^{-2}	9.78×10^{-5}	2.01×10^{-2}
1×10^6	7.27×10^{-3}	2.26×10^{-6}	1.97×10^{-2}	9.84×10^{-5}	2.21×10^{-2}

known to be efficient later than 100 years [26]. Figure 14 also highlights differences between the two solution methods. On the one hand, the total amount of CO_2 is not conserved in the sequential strategy. A difference of 2.73% is measurable between the total quantity of CO_2 and the exact quantity injected. On the other hand, the total mass of CO_2 computed by the fully implicit approach perfectly matches the exact value injected.

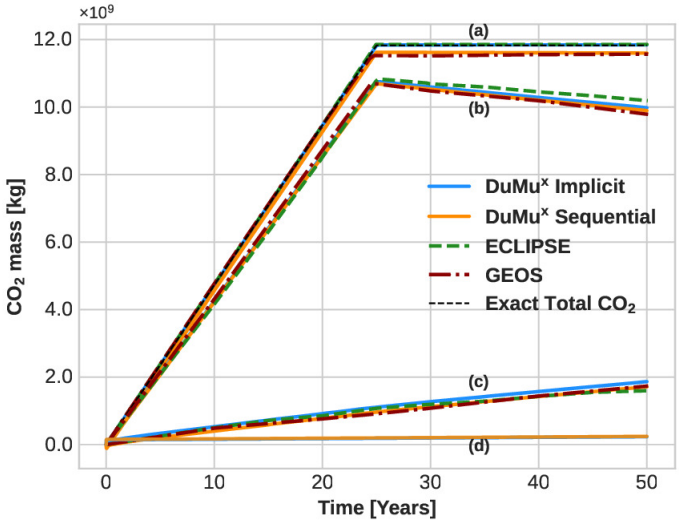

Figure 14: Evolution of CO_2 quantities as a function of time. (a) total injected mass of CO_2, (b) mass of CO_2 in gas phase, (c) mass of CO_2 dissolved in liquid phase, (d) mass of CO_2 in mineral phase

Performance comparison

We report runtimes separately for three stages of time integration: linearization and assembly of the linear system (Jacobian matrix and residual vector), solving the linear system, and updating the variables. The individual runtimes are accumulated over all Newton-Raphson iterations needed until convergence. Figure 15 (a) shows the evolution of these three computational times throughout the simulation. The main difference between the sequential and fully implicit approaches is due to the solving step. Indeed, as shown in the inset in Fig. 15 (a) for the implicit scheme, the computational time for the solving step is thirteen times higher than that of the sequential scheme (approximatively 13000 s versus 1000 s), while the other times are comparable or negligible. In Fig. 15 (b), we can see that the two approaches use very similar time step sizes. Figure 15 (c) displays the number of Newton iterations per time step for each approach. For the sequential one, this number corresponds to the sum of the number of Newton iterations for each subproblem: two-phase nonisothermal flow

and reactive transport. This cumulative number of iterations for the sequential approach is larger than for the implicit approach. Finally, the longer time for the solving step can be explained thanks to Fig. 15 (d), where it can be observed that the total number of linear iterations per time step is larger for the implicit approach. Computation for the inversion of the system in the fully implicit approach is much more expensive in terms of CPU time. This can be explained mainly by two reasons. First, for each Newton iteration, two linear systems must be solved in the sequential approach versus one for the implicit approach. Nonetheless, for the sequential approach, the size of the linear systems is smaller than the size of the linear system involved in the implicit approach. Second, for the implicit approach, the nonlinearities are stronger, particularly those due to saturation and temperature since all the equilibrium and kinetic chemical constants are temperature dependent. For the sequential strategy, nonlinearities of saturation and temperature are concentrated in the first linear system dedicated to the nonisothermal two-phase flow, while the second linear system dedicated to the reactive transport is solved at the imposed saturation and temperature. Heat transfer occurs slowly by conduction. This is why, at the beginning of the simulation, thermal effects do not play a major role in the nonlinearities of the linear systems, and the CPU time dedicated to the solving step is comparable for the sequential and implicit approaches. Both approaches use the same solver and preconditioner. Using a different preconditioner would surely be more beneficial to the implicit approach than to the sequential one. To conclude this comparison, we note that, despite a significant difference between sequential and implicit CPU times for the full simulation, the splitting error in the sequential scheme may also remain important. This error is very sensitive to the maximum time step size of the problem, and consequently, it is possible to minimize it.

Maximum time step size effect

To quantify the effect of the maximum time step on the mass conservation, we define the following quantity:

$$\varepsilon_{\mathrm{CO_2}} = \frac{|Tot_{inj}^{End} - Tot_{\mathrm{CO_2}}^{End} - Tot_{\Gamma_{Dir}}^{End}|}{Tot_{inj}^{End}}, \tag{23}$$

where Tot_{inj}^{End} represents the quantity of CO_2 injected at the final time, $Tot_{\mathrm{CO_2}}^{End}$ represents the total quantity of CO_2 present in the liquid, gas and mineral phases at the final time and $Tot_{\Gamma_{Dir}}^{End}$ is the cumulative flux of CO_2 across boundary faces where Dirichlet boundary conditions are imposed. Several simulations were carried out with different maximum time step sizes to investigate its effect on mass conservation using the original mesh. Table 10 represents the total computation time for several maximum time steps as well as the quantity $\varepsilon_{\mathrm{CO_2}}$, the total number of time steps, the average number of nonlinear iterations per time step and the average number of linear iterations per Newton iteration. As expected, the implicit scheme is perfectly mass conservative since the error $\varepsilon_{\mathrm{CO_2}}$ is close to the numerical precision. For the sequential approach, the error $\varepsilon_{\mathrm{CO_2}}$ is due to splitting errors and decreases with the time step. The implicit approach remains more accurate even if we take a smaller maximum time step size. For a given maximum time step, the number of time steps is comparable for the two approaches. As seen in Fig. 15, the number of Newton iterations for the sequential approach is larger than for the implicit approach, but the average number of linear iterations per Newton iteration is smaller for the sequential approach. Moreover, the size of the two linear systems to be solved for each subproblem of the sequential approach is smaller than the size of the linear system involved in the implicit approach. This may explain why the implicit approach takes longer than the sequential approach. Nonetheless, it is clearly visible that to reduce the splitting error of the sequential scheme and reach the same level as the implicit scheme, it is necessay to use smaller time steps. This obviously lengthens the computational time of the sequential approach, and the implicit approach can be faster in some cases if a certain precision is expected. Thus, the desired computational time and accuracy of the calculation can be an argument for the choice to use a sequential or implicit method.

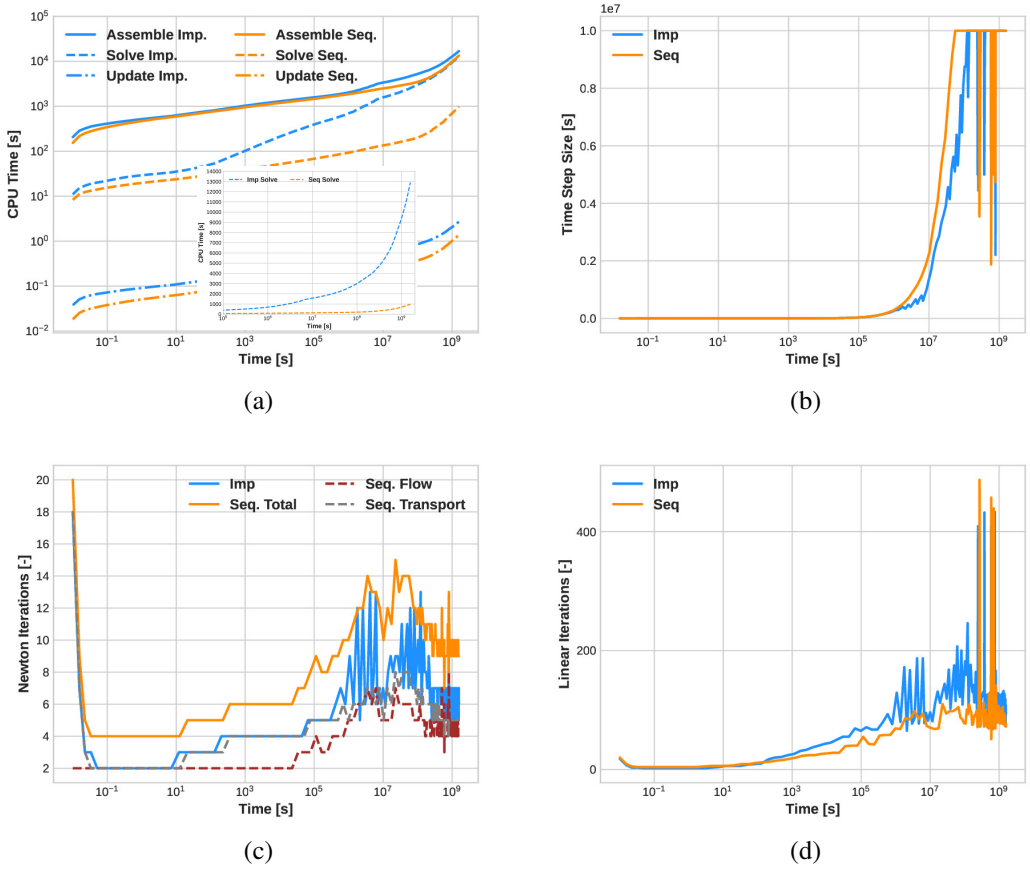

Figure 15: Comparison between the implicit and sequential approaches: (a) CPU time evolution as a function of the simulation time for different stages of the computation, (b) time step, (c) number of Newton iterations per time step, (d) total number of linear iterations per time step

Table 10: Numerical performances. CPU: elapsed time, TS: number of time steps, NI: average number of nonlinear iterations per time step, LI / NI: average number of linear iterations per Newton iteration

Method	dt_{max} [s]	CPU	TS	NI	LI/NI	ε_{CO_2}
Implicit	1×10^7	9h20min	236	6.37	15.89	1.02×10^{-14}
Implicit	5×10^6	12h03min	376	5.25	15.55	2.99×10^{-14}
Implicit	1×10^6	35h42min	1626	3.64	15.61	1.40×10^{-13}
Sequential	1×10^7	5h50min	222	8.63	9.41	2.73×10^{-2}
Sequential	5×10^6	7h19min	373	8.34	8.41	1.89×10^{-2}
Sequential	1×10^6	24h27min	1620	6.18	8.26	1.39×10^{-2}

4.3.4 High-performance computing

Complex calculations or large-scale simulations can be very time-consuming. High-performance computing helps to decrease the computational costs of a numerical simulation. The grid is partitioned thanks to a domain decomposition method, and all processors perform their own calculation simultane-

ously. The processors communicate via calls to MPI routines. This section compares more specifically the performance of the sequential and fully implicit approaches, and several specific terms need to be defined.

First, we define the speedup S_p and the ideal speedup S_p^{ideal} as

$$S_p = \frac{T_{base} p_{base}}{T_p} \quad \text{and} \quad S_p^{ideal} = \frac{p}{p_{base}}, \tag{24}$$

where p_{base} and T_{base} are the number of processors and CPU time taken as reference, respectively. p and T_p are the variable number of processors and the associated CPU time, respectively. These quantities allow us to define the behavior of the CPU time for different configurations.

It is also possible to define the strong scaling efficiency as

$$E_s(p) = \frac{S_p}{S_p^{ideal}}. \tag{25}$$

E_s is useful to define how the simulation time varies with the number of processors for a fixed-size problem. The strong scaling efficiency reflects the ideal behavior of the algorithm's parallelism. An ideal efficiency (close to one) indicates that interprocessor communications and synchronizations using the MPI protocol are negligible and that for a number of processors p, the CPU time would be almost divided by p.

Parallel performances

The initial mesh of 54756 cells was refined to obtain two meshes with 876096 and 3504384 cells that were used to run parallel simulations on up to 256 processors. All computations were carried out for the first year of the simulation. This period includes part of the simulation where the linear solver for the implicit method starts to deteriorate. Figure 16 (a) shows the CPU time evolution with respect to the number of processors for the two problem sizes. Fully implicit and sequential CPU times are significantly different since the fully implicit approach is at least twice as long as the sequential approach, regardless of the configuration. The more we increase the number of processors, the more CPU time deviates from the ideal behavior. Figure 16 (b) represents the strong scaling efficiency. For the smaller mesh, the communication overload is mainly due to the workload per processor becoming too low, leading to a rapid decrease in efficiency, especially for the implicit scheme. For the larger mesh, the workload seems sufficient, and a good efficiency is observed for both sequential and implicit schemes. The comparison of the efficiency of two different numerical methods is difficult. Indeed, the size of the linear problems to be solved and their complexity are different for the sequential and implicit schemes, leading to different communications for each scheme. Figures 16 (c) and (d) give a more detailed representation of the three main steps of the computation for the two different meshes. As seen before in Fig 15, the main difference between the CPU times for sequential and implicit approaches concerns the solving step since there is an order of magnitude between the time consumed by both approaches for this step.

4.3.5 Long-term evolution of CO_2

As mentioned in [26], mineral trapping only occurs over long timescales. For this reason, we considered longer simulation times to capture the mineralization phenomena. Nevertheless, the initial benchmark was not configured for a long-term simulation, as the CO_2 plume tends to disappear when it reaches the domain borders where Dirichlet boundary conditions are applied. Therefore, we modified these boundary conditions to contain the CO_2 plume within the domain without any leakage. We imposed homogeneous Neumann boundary conditions except on a single side located on the front side.

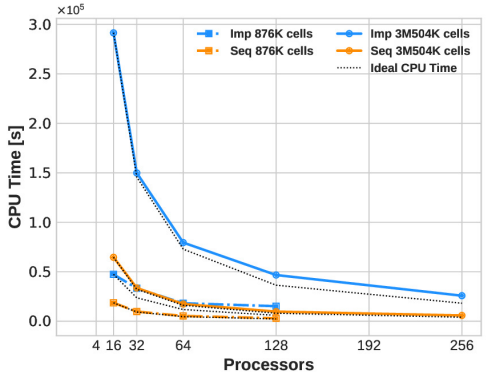

(a) CPU time

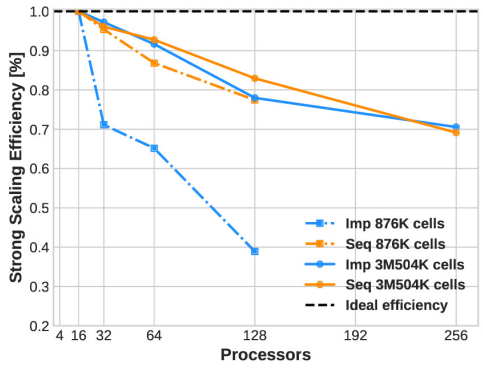

(b) Strong scaling efficiency

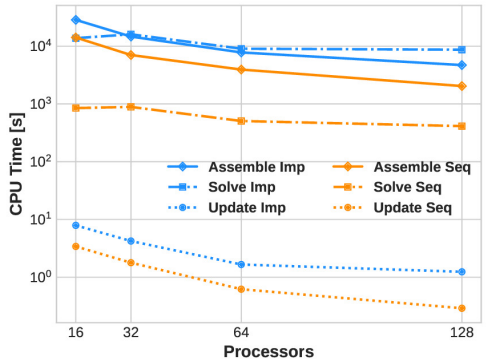

(c) Detailed CPU time for the mesh composed of 876096 elements

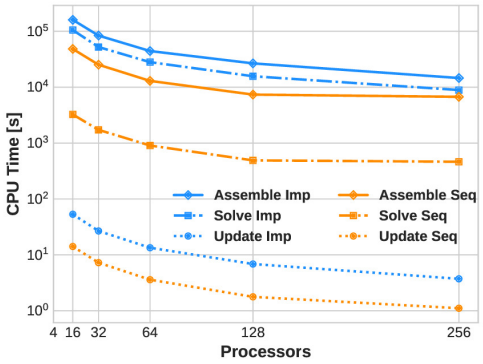

(d) Detailed CPU time for the mesh composed of 3504384 elements

Figure 16: Evolution of quantities with respect to the number of processors: (a) CPU time, (b) strong scaling efficiency, (c) detailed CPU time for the mesh composed of 876096 elements, (d) detailed CPU time for the mesh composed of 3504384 elements

Specifically, the simulation time is extended to 300 years to capture stronger mineralization effects. Mineral dissolution/precipitation may affect the porosity of the rock matrix. More precisely, the porosity ϕ depends on the concentrations of the minerals according to the relationship

$$\phi = \phi_0 - \sum_{j=1}^{N_m} v^j (c_s^j - c_{s,0}^j), \tag{26}$$

where ϕ_0 is the initial porosity, N_m is the number of reactive minerals, and v^j represents the molar volume [$m^3.mol^{-1}$] for mineral j. Finally, c_s^j and $c_{s,0}^j$ are the current and initial molar concentrations of mineral j [$mol.m^{-3}$] in the solid phase, respectively. The Kozeny-Carman relationship is used to address the porosity dependence of the permeability

$$\mathbb{K} = \mathbb{K}_0 \left(\frac{1-\phi_0}{1-\phi} \right)^2 \left(\frac{\phi}{\phi_0} \right)^3, \tag{27}$$

where $\mathbb{K}_0$ is the initial permeability.

The simulation is run with the implicit approach and a maximum time step $dt_{max} = 5 \times 10^6 s$.

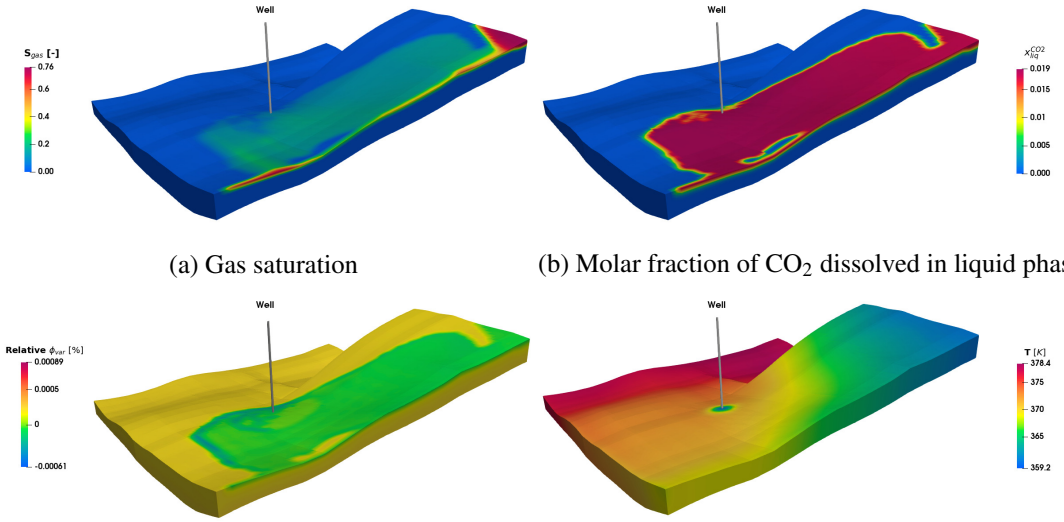

(a) Gas saturation

(b) Molar fraction of CO_2 dissolved in liquid phase

(c) Relative varation of porosity

(d) Temperature

Figure 17: Simulation results at $t = 300$ years

As shown in Fig. 17 (a), the gaseous CO_2 plume moves toward the upper part of the domain due to buoyancy. The Neumann boundary condition acts as a barrier preventing any leakage and inducing an accumulation zone of gaseous CO_2. However, the long-term movement of the plume increases the contact surface between CO_2 dissolved in the liquid phase and the host rock, as shown in Fig. 17 (b). This enhances the dissolution/precipitation process as can be observed in Fig. 17 (c), where the shape of the relative variation in porosity is strongly correlated to the shape of dissolved CO_2. The temperature variations due to the injection period dissipate over time, so that the reservoir returns to its original state (see Fig 17 (d)). The evolution of CO_2 quantities is depicted in Fig.18. The blue curve representing the CO_2 dissolved in liquid phase increases drastically from 0 to 200 years and gradually stabilizes toward an upper limit. Mineral trapping starts later and cannot be captured in the initial configuration due to the short exposure times. As depicted by the green line, the amount of CO_2 transformed into calcite gradually increases and becomes increasingly important over time. After 300 years the amount of mineralized CO_2 represents approximatively 10% of the total amount, demonstrating the effectiveness of this long-term process in ensuring safer storage.

5 Conclusion

In this article, an extension of sequential and fully coupled fully implicit strategies to THC processes is proposed. For this, the mathematical formulation of nonisothermal multiphase multicomponent flow with reactive transport was exposed and discretized with an FV method. The implementation of both strategies was performed on the same DuMu^X simulation platform, which allowed us to validate our model on several numerical test cases involving CO_2 sequestration scenarios. Taking into account temperature effects leads to an increased dissolution of CO_2 and calcite in the near-well and CO_2 plume

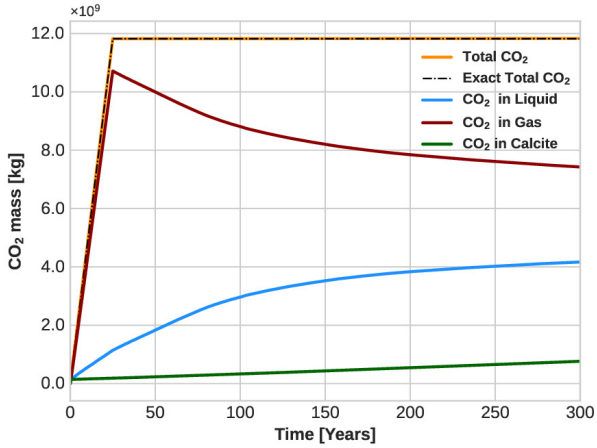

Figure 18: Long-term evolution of CO_2 quantities in the aquifer

regions, respectively. This can enhance both well injectivity and dissolution trapping. Comparisons between the sequential and fully implicit approaches have also been carried out, highlighting the fact that the fully implicit approach is mass conservative. The sequential approach introduces a splitting error that degrades the accuracy of the scheme despite a gain in calculation time. Furthermore, validations must be continued by considering other studies and benchmarks. Geomechanics is not taken into consideration in this study, but it should be considered for the assessment of the safety and durability of geological storage. Due to the localized temperature changes in the near-well regions, the latter should impact the mechanical effects more significantly. Finally, efforts have been made to provide a maximum of data and ensure the reproducibility of the tests performed in this study.

Acknowledgements

This research was carried out under the framework of the E2S-UPPA, Hub Newpores and Industrial Chair CO_2ES supported by the Investissements d'Avenir French programme managed by ANR (ANR16IDEX0002). We acknowledge financial support from E2S-UPPA, TOTAL Energies, BRGM and CNES. Computer time for this study was provided by CINES (allocation A0100610019 made by GENCI) but also with computer facilities from MCIA (Mesocentre de Calcul Intensif Aquitain) of the Universite de Bordeaux and of the Universite de Pau et des Pays de l'Adour.

References

[1] Chess database. https://thermoddem.brgm.fr/databases/chess

[2] DuMu^X Handbook (2023). https://dumux.org/docs/handbook/releases/3.7/dumux-handbook.pdf

[3] GEOS: Next-gen simulation for geologic carbon storage. www.geosx.org

[4] Open Porous Media initiative. http://opm-project.org/

[5] SINTEF (2009) Johansen data set. https://www.sintef.no/projectweb/matmora/downloads/johansen/

[6] Aavatsmark I, Eigestad G, Klausen R, Wheeler M, Yotov I (2007) Convergence of a symmetric MPFA method on quadrilateral grids. Computational Geosciences 11:333–345

[7] Abd A, Abushaikha A (2021) Reactive transport in porous media: a review of recent mathematical efforts in modeling geochemical reactions in petroleum subsurface reservoirs. SN Applied Sciences 3:401

[8] Ahusborde E, Amaziane A, El Ossmani M (2018) Improvement of numerical approximation of coupled two-phase multicomponent flow with reactive geochemical transport in porous media. Oil & Gas Science and Technology - Rev IFP Energies nouvelles 73

[9] Ahusborde E, Amaziane B, Id Moulay M (2021) High Performance Computing of 3D reactive multiphase flow in porous media: application to geological storage of CO_2. Computational Geosciences 25:2131–2147

[10] André L, Azaroual M, Menjoz A (2010) Numerical simulations of the thermal impact of supercritical CO_2 injection on chemical reactivity in a carbonate saline reservoir. Transp Porous Media 82:247–274

[11] Barrett R, Berry M, Chan T, Demmel J, Donato J, Dongarra J, Eijkhout V, Pozo R, Romine C, Van der Vorst H (1994) Templates for the Solution of Linear Systems: Building Blocks for Iterative Methods. Society for Industrial and Applied Mathematics

[12] Bastian P, Blatt M, Dedner A, Dreier N, Engwer C, Fritze R, Gräser C, Kempf D, Klöfkorn R, Ohlberger M, Sander O (2020) The DUNE framework: Basic concepts and recent developments. Computers & Mathematics with Applications 81:72–112

[13] Bastian P, Blatt M, Scheichl R (2012) Algebraic multigrid for discontinuous galerkin discretizations of heterogeneous elliptic problems. Numerical Linear Algebra with Applications 19

[14] Brunner F, Knabner P (2019) A global implicit solver for miscible reactive multiphase multicomponent flow in porous media. Computational Geosciences 23:127–148

[15] Bundschuh J, Al-Khoury R (2014) Geological CO_2 sequestration and compressed air energy storage - An introduction. CRC Press, 1–8

[16] Class H, Ebigbo A, Helmig R, Dahle H K, Nordbotten J M, Celia M A, Audigane P, Darcis M, Ennis-King J, Fan Y, Flemisch B, et al. (2009) A benchmark study on problems related to CO_2 storage in geologic formations. Computational Geosciences 13:409–434

[17] Ershadnia R, Wallace C, Hajirezaie S, Hosseini S, Nguyen T, Sturmer D, Dai Z, Soltanian M (2021) Hydro-thermo-chemo-mechanical modeling of carbon dioxide injection in fluvial heterogeneous aquifers. Chemical Engineering Journal :133451

[18] Eymard R, Gallouët T, Guichard C, Herbin R, Masson R (2014) TP or not TP, that is the question. Computational Geosciences 18:285–296

[19] Fan Y, Durlofsky L J, Tchelepi H A (2012) A fully-coupled flow-reactive-transport formulation based on element conservation, with application to CO_2 storage simulations. Advances in Water Resources 42:47–61

[20] Gan Q, Candela T, Wassing B, Wasch L, Jun L, Elsworth D (2021) The use of supercritical CO_2 in deep geothermal reservoirs as a working fluid: Insights from coupled thmc modeling. International Journal of Rock Mechanics and Mining Sciences 147:104872

[21] Kala K, Voskov D (2020) Element balance formulation in reactive compositional flow and transport with parameterization technique. Computational Geosciences 24:609–624

[22] Koch T, Gläser D, Weishaupt K, Ackermann S, Beck M, Becker B, Burbulla S, Class H, Coltman E, Emmert S, Fetzer T, Grüninger C, Heck K, Hommel J, Kurz T, Lipp M, Mohammadi F, Scherrer S, Schneider M, Seitz G, Stadler L, Utz M, Weinhardt F, Flemisch B (2021) *DuMu*^{X} 3 – an open-source simulator for solving flow and transport problems in porous media with a focus on model coupling. Computers & Mathematics with Applications 81:423–443

[23] Kolditz O, Görke U-J, Shao H, Wang W, Bauer S (2016) Thermo-Hydro-Mechanical-Chemical Processes in Fractured Porous Media: Modelling and Benchmarking. Springer

[24] Lasaga A (1984) Chemical kinetics of water-rock interactions. Journal of Geophysical Research: Solid Earth 89(B6):4009–4025

[25] Logan S (1982) The origin and status of the Arrhenius Equation. Journal of Chemical Education 59:279–281

[26] Metz B, Davidson O, de Coninck H, Loos M, Meyer L (2005) IPCC special report on carbon dioxide capture and storage. Cambridge University Press, UK

[27] Millington R J, Quirk J P (1961) Permeability of porous solids. Transactions of Faraday Society 57:1200–1207

[28] Morel F, Hering J (1993) Principles and Applications of Aquatic Chemistry. John Wiley & Sons

[29] Newell P, Ilgen A (2018) Science of carbon storage in deep saline formations: process coupling across time and spatial scales. Elsevier

[30] Niemi A, Bear J, Bensabat J (2017) Geological Storage of in Deep Saline Formations. Springer

[31] Nishikawa I (2019) On large start-up error of BDF2. Journal of Computational Physics 392:456–461.

[32] Scheer D, Class H, Flemisch B (2021) Subsurface environmental modelling between science and policy. Springer

[33] Sin I, Corvisier J (2019) Multiphase Multicomponent Reactive Transport and Flow Modeling. Reviews in Mineralogy and Geochemistry 85(1):143–195

[34] Schneider M, Flemisch B, Helmig R (2017) Monotone nonlinear finite-volume method for non-isothermal two-phase two-component flow in porous media. Int. J. Numer. Meth. Fluids 84:352–381.

[35] Su P, Mayer K, Macquarrie KTB (2017) Parallelization of MIN3P-THCm: A high performance computational framework for subsurface flow and reactive transport simulation. Environmental Modelling & Software 95:271–289

[36] Su P, Mayer K, Macquarrie KTB (2021) MIN3P-HPC: A high-performance unstructured grid code for subsurface flow and reactive transport simulation. Mathematical Geosciences 53:517–550

[37] Tao J, Wu Y, Elsworth D, Li P, Hao Y (2019) Coupled thermo-hydro-mechanical-chemical modeling of permeability evolution in a CO_2 -circulated geothermal reservoir. Geofluids 2019:1–15

[38] Tutolo BM, Kong XZ, Seyfried WE, Saar MO (2015) High performance reactive transport simulations examining the effects of thermal, hydraulic, and chemical (THC) gradients on fluid injectivity at carbonate CCUS reservoir scales. International Journal of Greenhouse Gas Control 39:285–301

[39] Vilarrasa V, Rutqvist J (2017) Thermal effects on geologic carbon storage. Earth-Science Reviews 165:245–256

[40] Williams G, Chadwick R, Vosper H (2018) Some thoughts on Darcy-type flow simulation for modelling underground CO_2 storage, based on the Sleipner CO_2 storage operation. International Journal of Greenhouse Gas Control 68:164–175

[41] Xie M, Kolditz O, Moog H (2011) A geochemical transport model for thermo-hydro-chemical (THC) coupled processes with saline water. Water Resources Research 47

[42] Xu B, Nagashima K, DeSimone J, Johnson C (2003) Diffusion of water in liquid and supercritical carbon dioxide: An nmr study. Journal of Physical Chemistry A 107:1–3

[43] Xu T, Apps J, Pruess K (2004) Numerical simulation to study mineral trapping for CO_2 disposal in deep aquifers. Applied Geochemistry 19:917–936

[44] Zhang R, Winterfeld P, Yin W, Xiong Y, Wu Y (2015) Sequentially coupled THMC model for CO_2 geological sequestration into a 2D heterogeneous saline aquifer. Journal of Natural Gas Science and Engineering 27:579–615

[45] Zhang R, Yin X, Winterfeld P, Wu Y (2016) A fully coupled thermal-hydrological-mechanical-chemical model for CO_2 geological sequestration. Journal of Natural Gas Science and Engineering 28:280–304

[46] Zhao R, Cheng J (2015) Non-isothermal modeling of CO_2 injection into saline aquifers at a low temperature. Environ Earth Sci 73:5307–5316